JOURNAL OF MATERIALS SCIENCE 28 (1993) 5414–5425

Review
The engulfment of foreign particles by a freezing interface

R. ASTHANA,* S. N. TEWARI
Chemical Engineering Department, Cleveland State University, Cleveland, Ohio, USA

The interactions of second-phase particles, liquid droplets or gas bubbles with a solidification front form the basis of various materials synthesis and purification processes and the design of microstructures in cast metal-matrix composites, as well as frost heaving and biological cell interactions. The physical mechanisms of this interaction phenomenon are based upon surface thermodynamic factors, solidification parameters, and fluid dynamic effects such as fluid drag and buoyancy. An overview is presented of the role of various factors which determine the nature as well as the kinetics of foreign particle–solidification front interactions, and the current status and limitations of the various theoretical models of the phenomenon.

Nomenclature

V	Critical velocity for particle engulfment
L	Latent heat of fusion
a_0	Atomic radius
Ω	Atomic volume
D_l	Diffusion coefficient in the liquid
T	Temperature
R	Particle radius
ΔS	Entropy of fusion
ρ_s	Density of the solid
ρ_l	Density of the liquid
ρ_p	Density of the particle
k	Boltzmann's constant
Δv	Difference in the specific volumes of solid and liquid
G	Temperature gradient
h_0	Critical gap thickness
R_b	Radius of surface bump on particle
σ_{sl}	Surface energy of solid–liquid interface
σ_{pl}	Surface energy of particle–liquid interface
σ_{sp}	Surface energy of solid–particle interface
μ	Viscosity of the melt
g	Acceleration due to gravity
$\Delta\rho$	Density difference between particle and liquid
A	Hamaker constant
B	$A/6\pi$
K_p	Thermal conductivity of the particle
K_l	Thermal conductivity of the liquid
C	Bulk concentration of the liquid
m_l	Slope of liquidus line
K_c	Partition coefficient
C_p	Specific heat of the particle
C_l	Specific heat of the liquid

1. Introduction

When a liquid containing insoluble foreign particles is solidified, the solidification front may interact with the suspension of particles in one of three distinct modes: the front may engulf a particle instantaneously upon contact, the front may push the particle indefinitely and segregate it in the last-freezing liquid, or the front may engulf the particle after pushing it over some distance. Such interactions of foreign particles with a freezing interface are encountered in a wide range of physical processes such as materials synthesis (solidification of monotectics [1] and metal-matrix composites [2–6], inclusion control during growth of crystals [7]), separation processes [8, 9], frost heaving [10] and biological cell interactions [11]. Thus, from a mechanical properties perspective, the microstructures of cast metal-matrix composites reinforced with ceramic particulates require a uniform distribution of reinforcing phase in the matrix of a continuous primary metallic phase. The solidification process should, therefore, preserve (at a scale comparable to the scale of the microstructure) the original homogeneous distribution of particles in the premixed melt–particle suspension, i.e. the front should be oblivious to the presence of the particles. On the other hand, control of inclusions during casting of metals and growth of impurity-free-crystals demands a purification role for the solidification front, i.e. the solid must selectively reject the impurities. Past studies (Table I) from various disciplines concerned with change of phase from liquid to solid have documented observations on the interactions of particles, liquid droplets and gas bubbles with freezing interfaces in various liquids.

*Mailing address: MS 105-1, NASA Lewis Research Center, Cleveland, OH 44135, USA.

0022–2461

TABLE I Experimental studies on particle–front interactions in different systems

Particle	Matrix	Reference
Pb droplets (20–50 μm)	Hypermonotectic Cu-Pb alloys	[2]
Ga droplets	Bi–50% Ga alloys	[12]
SiC (25–100 μm)	Al–2% Mg, Al–6% Ni	[13]
SiC (~ 10 μm)	Al–Si (A356 and 6061)	[2]
Cu (5–48 μm)	Ice-water	[14]
Nylon, acetal, PMMA (10–100 μm)	Naphthalene, biphenyl, Salol	[15]
Ag, Al, Cu, W, silica	Salol, water	[16]
Glass, Al, W, Ta, Mo, Fe, Ni, Cr (< 1000 μm)	Naphthalene, Bi, Sn, Zn	[17]
C, MgO, Si, Sn, Fe_2O_3, Ni	Orthoterphenyl, Salol, Thymol	[18]
Al_2O_3, Si, Mo, W (1–1000 μm)	Cu, Al	[19]
SiC, C, glass, Al_2O_3	Al, Al–Si, Al–Cu alloys	[5, 6]
SiC, Al_2O_3	Mg, Mg alloys (AZ 91, 31 and 61)	[20]
Fe	Pb–Sn	[21]
Al_2O_3, SiC, TiB_2, ZrB_2, B_4C	Al–Mg	[3]
Mica, shale, quartz, rutile (~ 500 μm)	Ice-water	[10]
C, Si, Cu	Naphthalene, Salol, camphor, benzophenone	[9]
Fe coated with Au, Ag, Al	Salol	[8]
Pyrex (~ 100 μm)	Ice-water	[22]
Latex (3–7 μm)	Ice-water	[23]
Al_2O_3, Co, Ni (0.03–100 μm)	SCN	[24, 25]
Ni	SCN, Salol	[26]

The interaction phenomenon has also been analysed theoretically to identify the underlying mechanisms, and to make predictions of conditions (e.g. solidification rate) which may lead to a particular type of interaction behaviour. While the earlier studies treated the interaction phenomenon primarily as a theoretically interesting problem, recent studies have focused on its relevance to the design of microstructures in advanced materials such as cast metal-matrix composites. The various studies have either measured (or predicted) the minimum pressure (crystallization pressure) on a solid which is necessary to stop the growth of the solidification front approaching the solid [27], or measured the velocity (critical or transition velocity) of the front above which an inclusion is engulfed by the front [14, 15, 18, 22]. Several theoretical models [13, 23, 28–41] of particle–interface interactions have been proposed in the literature to predict the critical velocity for particle engulfment. Each of these models applies to some aspects of the phenomenon, and explains some of the experimental data. The models differ from each other mainly in the mathematical sophistication (e.g. the boundary conditions that the solidification front must satisfy) and the method of solution, but use a similar approach (e.g. balance of repulsive and attractive forces between particle and the front) to describe the process of interaction.

The purpose of this paper is to present an overview of the physical principles that govern the capture and rejection of inclusions by a freezing interface, and to briefly discuss the usefulness and limitations of the various theoretical models of the interaction phenomenon. The role of particle–front interactions in the solidification synthesis of metal-matrix composites has been discussed in earlier studies [2–6, 24, 25, 41, 42], and a comprehensive evaluation of various theoretical models against published data in various systems has been attempted [43].

2. Physical basis of interactions

2.1. Surface energy

The engulfment of a particle suspended in a melt by a freezing interface requires replacement of two interfaces (particle–liquid and liquid–solid) by a single interface (solid–particle) (Fig. 1). Since each of these interfaces has a tension (interfacial tension) associated with it, the above process of interface substitution must be energetically favourable for engulfment of particles to be spontaneous. From a thermodynamic point of view [15, 28], engulfment is spontaneous when $\Delta G_{net} < 0$, and it is unfavourable when $\Delta G_{net} > 0$. The total free energy change during the process of engulfment is $\Delta G_{net} = \sigma_{sp} - \sigma_{pl}$, where σ_{sp} and σ_{pl} are the specific surface energies of the solid–particle and particle–liquid interfaces, respectively. Alternatively, the free energy of adhesion, $\Delta G_{adh} = \Delta\sigma_0$ ($= \sigma_{sp} - \sigma_{pl} - \sigma_{sl}$) must also be negative for engulfment to be spontaneous. At slow growth rates and in the absence of external (body) forces, the engulfment or rejection of particles by a freezing interface can therefore be qualitatively predicted on the basis of the above thermodynamic criterion. Fig. 2 shows typical values of the free energy change $\Delta\sigma_0$ for several organic systems from the work of Neumann and co-workers [15, 28]; in all the cases where $\Delta\sigma_0 < 0$, the particles were engulfed by the front

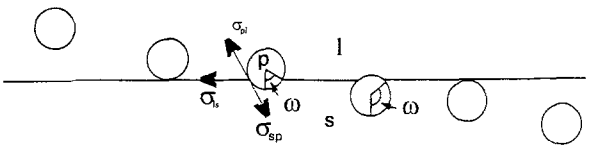

Figure 1 Schematic diagram showing process of engulfment of a sphere by a planar solid–liquid interface (l-liquid, s-solid and p-particle). ω denotes the semi-apical angle for engulfment of the sphere and σs represent the specific surface energies of subscripted interfaces between solid, liquid and particle, respectively.

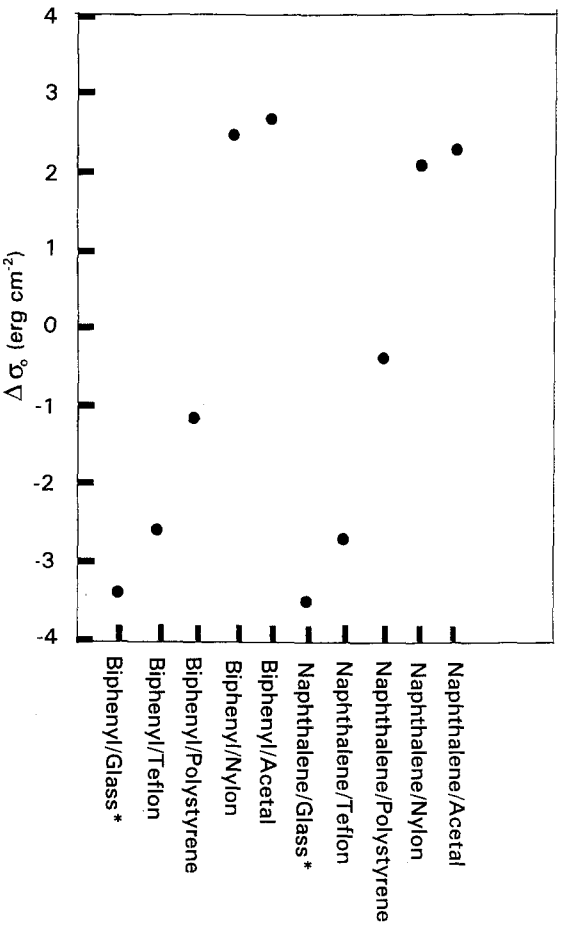

Figure 2 Estimated values of the driving force for repulsion, $\Delta\sigma_0$, in various organic systems [15, 28]; (*) data for siliconed glass. 1 erg $= 10^{-7}$ J.

whereas they were rejected by the front in all the cases where $\Delta\sigma_0 > 0$. The free energy of adhesion can be determined from measurements of the critical velocity V by using the following relationship obtained from a dimensional analysis [28]:

$$Re = h\left(\frac{\Delta G_{Adh}}{\rho_p C_p D T}\right)^l \left(\frac{\Delta G_{Adh}}{\mu^{1/2} K_p T}\right)^m (Le)^n \qquad (1)$$

where Re ($= \rho_l VD/\mu$) is the Reynolds number, ΔG_{adh} is the free energy of adhesion, Le ($= D_l C_l \rho_l / K_l$) is the Lewis number of the melt, h, l, m and n are system constants, ρ_p and ρ_l are particle and melt densities, C_p and C_l are specific heats of particle and melt, K_p and K_l are thermal conductivities of particle and melt, and μ, D and T are melt viscosity, particle diameter and temperature, respectively. The constants h, l, m and n are obtained from calibration experiments [28]. Alternatively, Equation 1 can be used to predict V in systems with known ΔG_{Adh}, which necessitates independent determination of various surface energies. While σ_{sl} and σ_{lp} may be determined using the standard techniques such as sessile drop test and nucleation experiments, the determination of σ_{sp} is the most difficult, and experimental measurements are virtually non-existent [44, 45]. Theoretical approaches such as an equation of state have been proposed [28] for low-energy solids (surface energy < 70 mJ m^{-2}) to estimate the various interfacial energies, including σ_{sp}. Thus any combination of interfacial energies between three phases (1, 2 and 3) may be determined from the following generic equation:

$$\sigma_{12} = \frac{(\sigma_{13}^{1/2} - \sigma_{23}^{1/2})^2}{1 - K\,\sigma_{13}^{1/2}\,\sigma_{23}^{1/2}} \qquad (2)$$

where the constant $K = 0.015$ for organics [28] and 0.001 for metals [45]. The above approach has been successfully utilized by Neumann and co-workers in studying particle pushing; however, estimates of σ are not always reliable [40]. For example, the solid–liquid interfacial energies (σ_{sl}) of naphthalene and biphenyl are estimated from the above approach to be 0.59 and 0.64 mJ m^{-2} whereas the experimental values of these energies [40] are two orders of magnitude larger (61 ± 11 and 50 ± 10 mJ m^{-2}, respectively). On the other hand, even with known surface energies, the thermodynamic criterion can only make qualitative predictions of pushing–engulfment transitions and is at best applicable to experiments involving slow growth rates and negligible body forces.

The application of a thermodynamic criterion requires a knowledge of the interfacial energies σ_{sp}, σ_{lp}, and σ_{sl}. While the sign of the overall change in $\Delta\sigma_0$ indicates the thermodynamic feasibility of engulfment or rejection, the actual energetics of the process of engulfment (after the initial contact is established between the front and the particle) is dependent on the path of the process. Computations of the energetics of the process of particle engulfment by a solidification front based on a generic analysis [46, 47] for transfer of a solid across an interface between any two phases (liquid–liquid, liquid–vapour, liquid–solid) show (Fig. 3) that the process of engulfment could be an uphill task after partial engulfment, even though the overall process is thermodynamically favourable.

For pushing to occur, a liquid film must always occupy the gap between the particle and the solidification front; hence, the stability of a liquid film between two solids is an important consideration in particle pushing. Studies on the stability of thin films [40, 48] postulate the existence of a disjoining pressure, which is essentially a jump in the pressure at each of the solid surfaces supporting the film. This disjoining pressure has its genesis in various forces such as ionic electrostatic forces (overlapping of double ionic layers), dispersion or molecular forces (van der Waals), structural forces (structural modification of the film due to surface forces), and adsorption due to dissolved molecules. The disjoining pressure Π is related to surface energy from [40]

$$\frac{\delta\Pi}{\delta h} = \frac{1}{h}\left(\frac{\delta\sigma}{\delta h}\right) \qquad (3)$$

and for thin films

$$\Pi = \frac{A}{6\pi h^3} \qquad (4)$$

where h is the film thickness and A is the non-retarded molecular force (Hamaker) constant. Substituting Equation 4 in Equation 3 and integrating the resulting

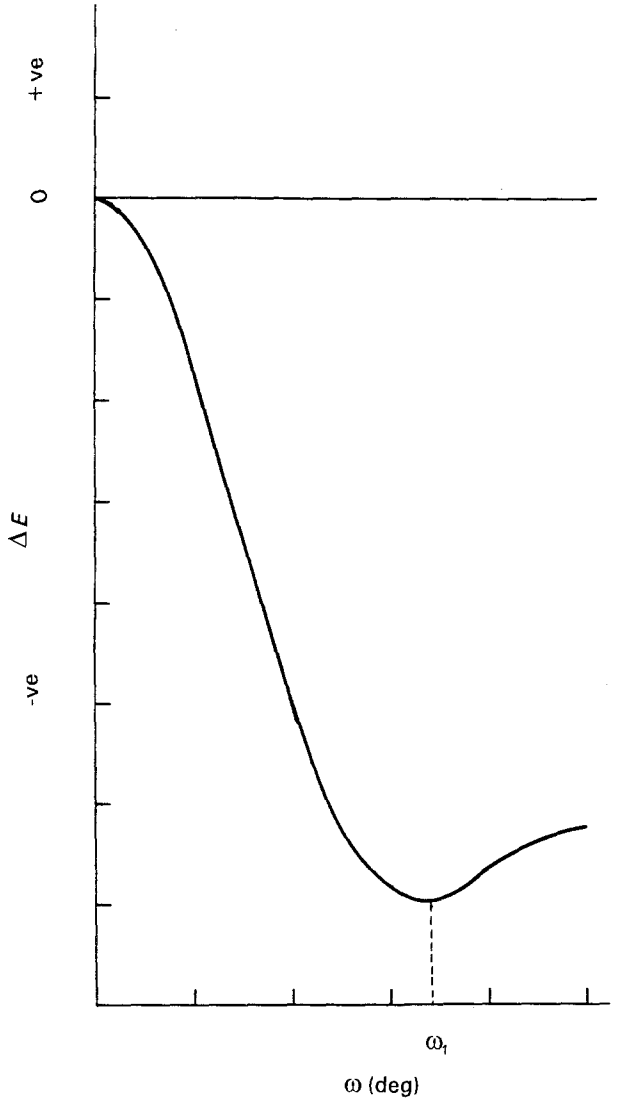

Figure 3 Schematic variation of the surface energy ΔE for particle engulfment by a freezing interface with the semi-apical angle ω for engulfment. Note that engulfment beyond ω_1 is an uphill task, even though the overall change in the free energy is negative.

expression from $\sigma = \sigma_{sl} + \sigma_{lp}$ at $h = \infty$ to $\sigma = \sigma(h)$ yields

$$\sigma(h) = \sigma_{sl} + \sigma_{lp} - \frac{A}{4\pi h^2} \tag{5}$$

Representing $\sigma(h) - (\sigma_{sl} + \sigma_{lp})$ by $\Delta\sigma$ and $-A/4\pi h_0^2$ by $\Delta\sigma_0$ yields

$$\Delta\sigma = \Delta\sigma_0 \left(\frac{h_0}{h}\right)^2 \tag{6}$$

This expression shows that the surface energy of a thin liquid film is a function of its thickness. A continuous variation of $\Delta\sigma$ with separation h has been assumed in the above expression (Fig 4), since $\sigma_{sl} + \sigma_{lp}$ must approach σ_{sp} at $h = h_0$. The thickness dependence of the surface free energy of the liquid film is reasonable to assume if the structure of the liquid changes over a few molecular diameters near the interface, since then the chemical potential will be a function of distance. The chemical potential of the film can be expressed as a summation of a bulk part, μ_b, and a thickness-dependent part, $g(h)$, i.e. $\mu = \mu_b + g(h)$, where the function $g(h)$ is either a power function or an exponential

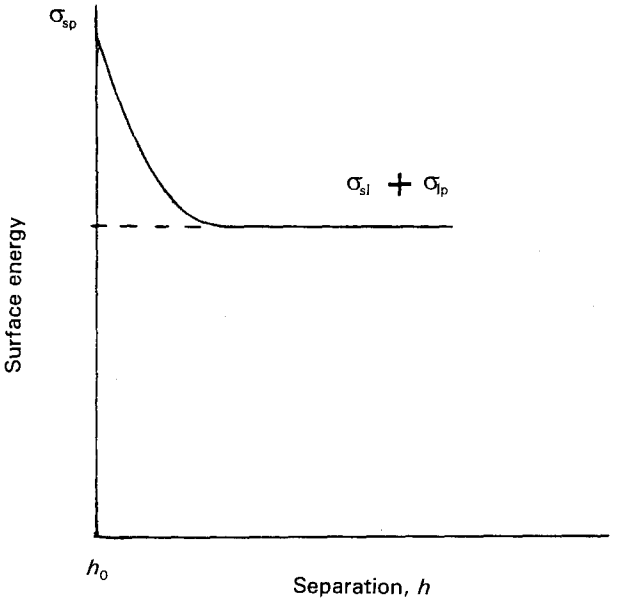

Figure 4 Schematic variation of surface energy with separation between the particle and the solidification front [18].

function of film thickness [31]. The above derivation shows the equivalence of disjoining pressure and surface energy approaches, provided the molecular force constant A is related to the surface energy function by $A = 4\pi h_0^2 \Delta\sigma_0$, where h_0 is of the order of several molecular diameters.

In order to develop a kinetic model of interaction phenomena, it is necessary to consider a position-dependent surface energy (or equivalently, a film thickness-dependent disjoining pressure), such that the change in chemical potential of the liquid film in the contact region with decreasing separation between the solidification front and the particle can be related to the transport processes of fluid flow and diffusion that are required to feed the gap to maintain a stable film and thereby prevent particle capture. Theoretical models of particle pushing have been based both on the surface energy approach [18] and the disjoining pressure concept [31–34]. In the former, the net change in the surface free energy, $\Delta\sigma$, is taken as the driving force for diffusion of liquid in the gap. In the disjoining pressure approach, it is assumed that as the front approaches the particle, the film thickness in the contact region tends to be reduced; as a result the mean pressure around the rest of the particle forces a flow of liquid into the film so as to maintain an equilibrium thickness. The basic mechanism of pushing involves a balance of repulsive forces arising from the need to maintain a stable liquid film (which prevents contact and particle engulfment) and the attractive forces (e.g. fluid drag) which compress the particle toward the front during growth and therefore favour engulfment. The particle, initially at rest, is accelerated ahead of the advancing solidification front when the width of the gap between the two becomes comparable to the size of the zone of strong interactions. This repulsive interaction is countered by the viscous drag on the particle; a steady-state behaviour corresponding to pushing at a constant velocity may eventually be reached if a critical thickness of the liquid film can

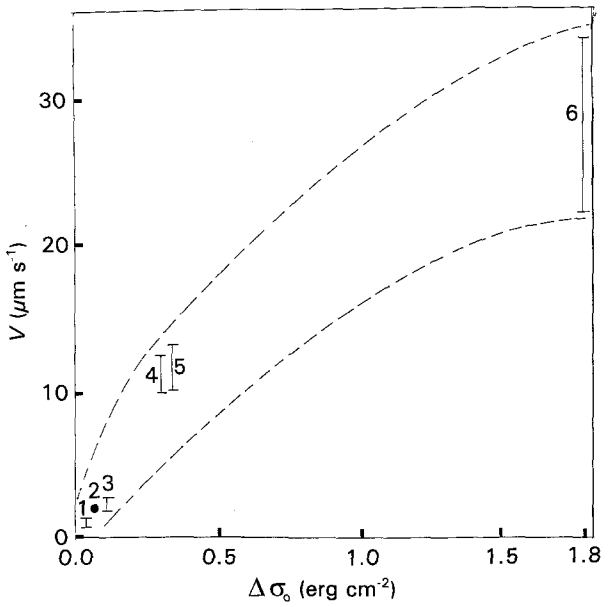

Figure 5 Dependence of critical velocity for particle engulfment on the driving force for repulsion, $\Delta\sigma_0$: (1) Salol–PMMA, (2) Salol–nylon, (3) Salol–acetal, (4) biphenyl–PMMA, (5) naphthalene–PMMA, (6) biphenyl–nylon. Data are for particles of diameter 20 μm; (●) denotes mean value. 1 erg = 10^{-7} J.

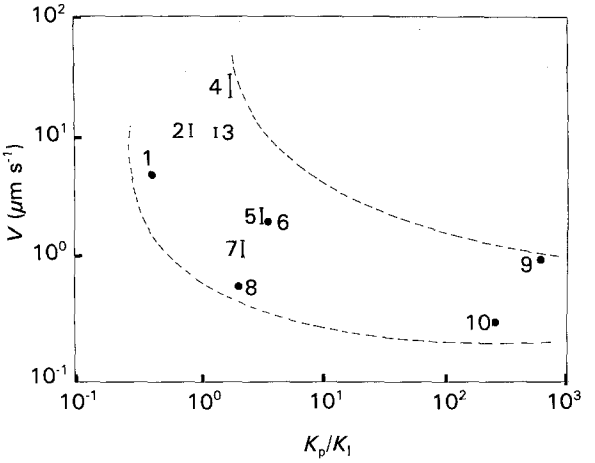

Figure 6 Dependence of critical velocity for particle engulfment on the ratio K_p/K_l: (1) latex–water, (2) naphthalene–PMMA, (3) biphenyl–PMMA, (4) biphenyl–nylon, (5) Salol–acetal, (6) Salol–nylon, (7) Salol–PMMA, (8) silica–water, (9) Cu–water, (10) tungsten–water. Data are for 20 μm diameter particles; (●) denotes the mean value.

be maintained in the gap region, the dimensions of which are predicted to be on the order of 10^{-6} cm. The critical gap thickness is, however, a somewhat ill-defined parameter in most models and it may be an order of magnitude smaller for sufficiently fine particles [32]. Also, for a planar front in a pure melt the critical gap thickness could approach a few molecular diameters [29].

Since the particle interferes with the transport processes, the local growth velocity of the front behind the particle is altered. The front therefore acquires a net curvature, which in turn leads to a change in the melting point or a change in the free energy of fusion. The shape of the perturbation in the front that develops under the particle can be determined from the relationship between the interface temperature and kinetic undercooling, the Gibbs–Thompson curvature term, temperature changes associated with external forces (e.g. gravity) and fluid drag. Since the repulsive forces arise from the need to maintain a stable film, the surface energy term $\Delta\sigma_0$ provides the driving force for repulsion; a larger value of $\Delta\sigma_0$ makes engulfment more difficult and hence a higher front velocity is required to engulf the particles in systems having a large value of $\Delta\sigma_0$, as shown in Fig. 5.

2.2. Thermal effects

The growth of a liquid–solid interface in a pure melt under a positive temperature gradient (with heat extraction taking place through the growing solid) is governed by the gradient G of temperature in the melt at the interface. Foreign matter with thermal properties different from those of the melt can distort the gradient locally, by serving as local thermal resistances. For smooth particles and faceted solid–liquid interfaces, thermal effects are dominant at large (> 500 μm) particle sizes, whereas curvature effects (interface energy) dominate at fine (< 500 μm) particle sizes [32]. Thus, in the case of relatively large particles in a positive temperature gradient, if $K_p < K_l$, the particle shields the local segment of the interface underneath the particle, resulting in a cooler spot and hence a faster growth velocity. This causes a convex protuberance to appear on the front underneath the particle. Since the hydrodynamic force favouring engulfment is expected to be lower in front of a convex surface compared to a concave or planar surface, the particle tends to be pushed by the convex protuberance. For $K_p > K_l$, the reverse is true and the particle is engulfed by a concave depression formed in the solidification front.

The ratio K_p/K_l affects the depth and the curvature of the depression; a larger value of the ratio leads to a deeper depression which promotes particle engulfment even at relatively low velocities, as shown in Fig. 6. Past experiments [25] have shown that this ratio can be used in making qualitative predictions of pushing and engulfment behaviour. Fig. 7 shows the value of thermal conductivity ratio (K_p/K_l) in several aqueous, organic and metallic systems in which particle–front interactions have been experimentally studied by various authors. In all the systems in which the thermal conductivity ratio is less than unity, particles were observed to be pushed by the front, whereas in systems where this ratio is greater than unity, the particles were engulfed by the front. The thermal conductivity criterion seems to work in most of the systems except some [17], and a later modification of this criterion [39] employs the ratio of the square roots of heat diffusivities of particle and liquid $(K_p C_p \rho_p/K_l C_l \rho_l)^{1/2}$ in place of the thermal conductivity ratio. This latter modification appears to correctly predict pushing–engulfment behaviour in all the systems in which it has been tested. The heat diffusivity ratio also enters the expression for critical velocity (Equation 1) derived from a dimensional analysis [28]. This can be seen by rearranging Equation 1 as

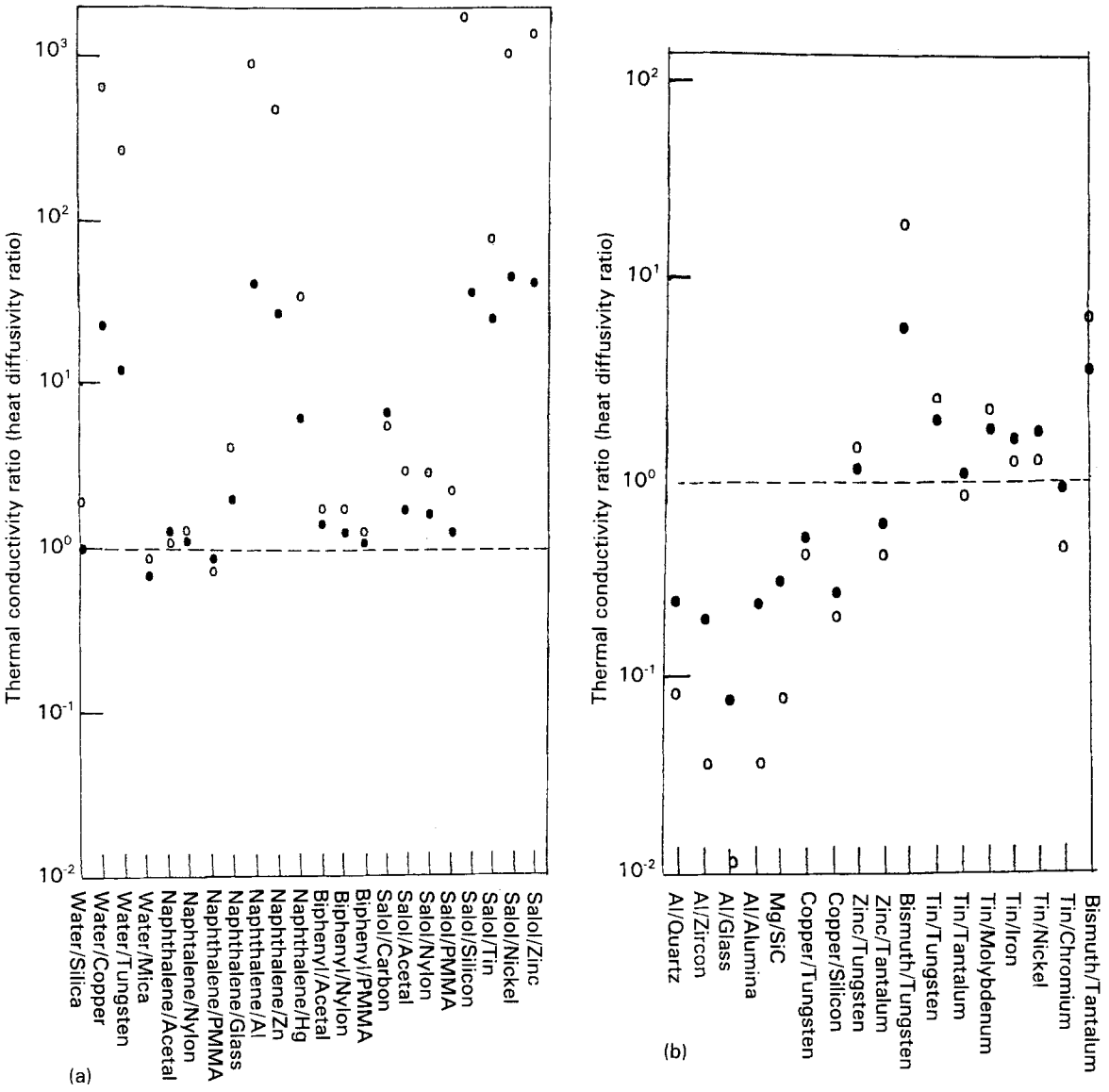

Figure 7 Predictions of pushing–engulfment transitions based on (○) thermal conductivity and (●) heat diffusivity criteria in several (a) non-metallic and (b) metallic systems.

follows:

$$V = A\left(\frac{K_p^{1-0.5m}}{K_l^{2n}}\right)\frac{(K_l C_l \rho_l)^n}{(K_p C_p \rho_p)^l} \qquad (7)$$

where A is a constant and the exponents h, l, m, and n are system-specific. While the heat diffusivity criterion was originally offered [39] as an empirical rule of thumb, the one-half power of the heat diffusivity ratio is reminiscent of the similar term in the expression for solidification kinetics in a mould, where the term represents the heat absorbing rate of the mould material [49].

Since the particles distort the thermal field ahead of the solid–liquid interface, the critical velocity for particle engulfment depends upon the temperature gradient in the melt (Fig. 8). Larger critical velocities are required to capture particles at larger values of temperature gradient at the solid–liquid interface. The actual dependence of V on G is, however, a function of several variables such as particle size and the thermal conductivities of particle and melt. Different theoretical models propose different functional dependences of V on G. Thus, Hoekstra and Miller [22] proposed that $V \propto G$, whereas Chernov *et al.* [32] showed that for $K_p = K_l$ $V \propto G^{0.25}$ for large ($R \gg 500$ μm) particles and V is independent of G for small ($R < 500$ μm) particles. For $K_p \neq K_l$, these authors showed [34] that $V \propto G^{-0.25}$. The experimental data from different studies sometimes show a conflicting behaviour for the dependence of V on G. Cisse and Bolling [14, 16] reported that a lower value of G led to an increase in V in their experiments; for instance, in the Cu–ice-water system, values of V at $G = 10\,^{\circ}\mathrm{C\,cm^{-1}}$ are 0.47, 0.6 and 1.7 $\mu m\,s^{-1}$ for Cu particles of average diameters 32.5, 20 and 5 μm, respectively, whereas the corresponding values of V at $G = 1\,^{\circ}\mathrm{C\,cm^{-1}}$ are 1.0, 1.2 and 2.4 $\mu m\,s^{-1}$, respectively. On the other hand, recent experimental work by Korber *et al.* [23] on the latex particles–ice-water system shows that V increases roughly linearly with G in qualitative agreement with the predictions of Hoekstra and Miller [22]. There is, however, a need to clarify the exact dependence of V on G by additional experimental and theoretical work.

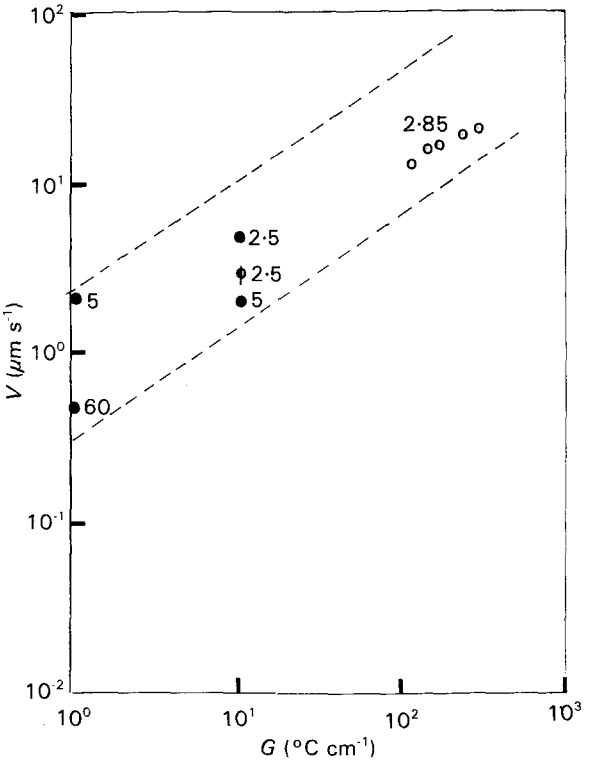

Figure 8 Experimental data showing dependence of critical velocity on temperature gradient in the melt at solid–liquid interface: (●) Cu–water [14], (◐) tungsten/water [14], (⊙) latex–water [23].

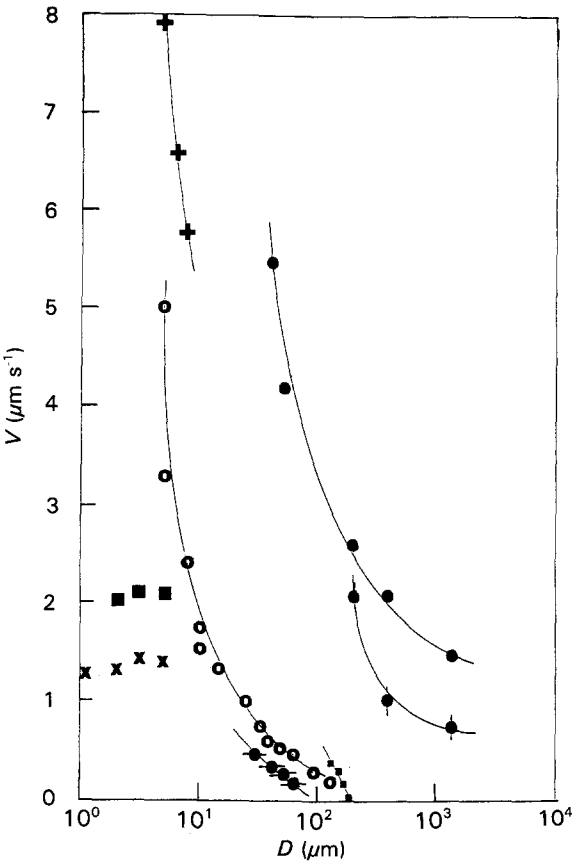

Figure 9 Experimental data from different studies showing variation of critical velocity with particle diameter: (■) diamond–Salol [18], (×) diamond–orthoterphenyl [18], (+) latex–water [23], (●) W–water [14], (○) Cu–water [14], (■) silica–water [14] (●) anthracite–water [17], (◆) glass–napthalene [17].

2.3. Viscous drag and buoyancy

Since the force of viscous drag on a particle during particle–front interactions is an attractive force favouring engulfment, larger particles (which experience greater drag) will be more easily engulfed than finer particles. In other words, the critical velocity for particle engulfment in a given system is larger for fine particles than for coarse ones (Fig. 9). Similarly, the attractive drag forces are larger on a particle in melts of higher viscosity; hence, lower capture velocities are required in melts of higher viscosity [18]. (The viscosity itself in thin liquid films is larger than that in the bulk; thus, μ for an aqueous solution of silica gel in fine capillaries 10^{-7} cm in diameter is 16 times the bulk value of viscosity [32].) For a sphere in front of a planar solid–liquid interface, the drag force is a function of particle radius, viscosity and front velocity, and is given by the expression [18]

$$F_d = 6\pi\mu V R^2/h \qquad (8)$$

Once the front begins to bend locally, the nature of liquid flow as well as drag force changes. The drag force compressing the particle toward a curved front depends upon the curvature of the solid–liquid interface behind the particle and is given by [37]

$$F_d = \frac{6\pi\mu V R^2}{(1-\alpha)^2 h} \qquad (9)$$

where the constant α characterizes the curvature of the front such that $\alpha = 0$ for a planar interface and $\alpha = 1$ for a hemispherical front. Grain boundaries and triple points are regions of concavity (depression) which are fed easily with the fluid compared to planar and convex interfaces; as a result the liquid film separating the particle from the front remains stable even at relatively high velocities, and the capture velocity increases (by factors of $2^{1/2}$ and $3^{1/2}$ for grain boundaries and grain junctions, respectively). Engulfment occurs when fluid flow in the gap between the curved front and the particle becomes insufficient to keep the thin liquid film from solidifying. Gas bubbles in melts require a higher velocity for their capture compared to solid particles of the same size, since the hydrodynamic forces compressing the second phase toward the front are larger on the bubble compared to a solid particle (the bubble–melt interface is in fact the free surface of the liquid) [34].

During solidification of particle–melt suspensions in a vertical configuration, buoyancy forces may assist or impede the process of particle engulfment depending upon the difference in the densities of particle and melt, and the direction (parallel or antiparallel to gravity) of movement of the front [4, 6, 13, 37, 38]. Thus, in countergravity growth (melt at top and solid at bottom) buoyancy forces will favour engulfment when $\rho_p > \rho_l$, and oppose engulfment when $\rho_p < \rho_l$. Mathematically, the contribution of buoyancy can be added to the attractive (drag) forces in deriving expressions for critical velocity. The buoyancy term (which varies with the cube of particle radius) is generally small for fine particles compared to the drag term (which varies as the square of particle radius) and may be neglected when the density differences are small. The shape and the volume fraction of particles

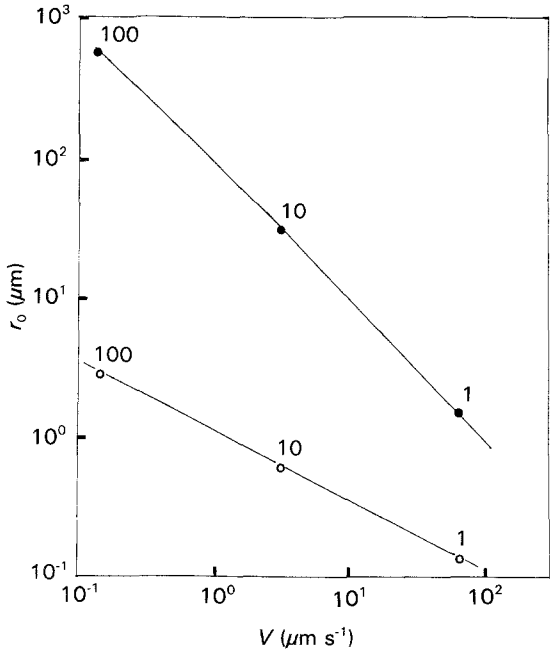

Figure 10 (○) Predictions of critical velocity V and radius r_0 of the zone of strong interaction for particles of 1, 10 and 100 μm radius in camphor, based on the model of Chernov *et al.* (after [40]). Also shown (●) are the scales (D_l/V) of the diffusion field for these particles at the corresponding velocities ($D_l = 10^{-6}$ cm^2 s^{-1}).

also affect the critical velocity for particle engulfment as well as the stability of the growth front. A larger volume fraction and a larger particle size also tend to be more effective barriers to solute fields ahead of the front, so that in both situations V is reduced compared to low volume fractions and finer particles.

2.4. Solute effects

Since growth from solutions depends upon the gradient of solute build-up at the solid–liquid interface, the obstruction of the diffusion field by the particles in front of the phase-change interface tends to reduce the concentration gradient at the interface, G_c; as a result the local growth velocity is reduced and a depression appears on the front which favours particle engulfment due to an increased drag force on the particle in front of a concave interface. Finer particles provide less obstruction to the solute build-up than coarse ones. For quasi-stationary interface growth under purely diffusive (non-convective) conditions, the concentration field can be described by the solution of the Laplace equation. An analysis for solution growth under these conditions shows that $V \propto R^{-2}$ whereas $V \propto R^{-4/3}$ for growth in a pure (unalloyed) melt [34]. The stationary interface solution is, however, valid when $D_l/R \gg V$, where D_l is the solute diffusion coefficient in the melt. Hence, the solution is limited to relatively low growth rates and fine particle sizes. For concentrated solutions and $K_p \neq K_l$, both thermal and solute fields affect the curvature of the interface and in this case, $V \propto G^{0.5}R^{-1}$ [32].

The curvature of the bent interface allows lateral solute diffusion and the interface tends to accelerate, leaving a solute-rich band around the particle which is engulfed. The solute fields are long-range (with a length scale of D_l/V) in contrast to the relatively short-range molecular interactions assumed in most models of particle–front interactions. Hence, during growth from solutions or alloys, the long-range solute field interactions with particles may dominate over the short-range molecular forces. Fig. 10 compares the dimensions of the zone of strong interaction in the gap between the particle and the front, based on van der Waals-type interactive forces, with the scale of the diffusional interactions at the corresponding critical velocities. Even for relatively pure melts, the diffusional interactions may be significantly larger than the short-range forces. However, the identification of purely diffusive (solute) effects during particle pushing may sometimes be difficult. Thus, Korber *et al.* [23] found no effect of solute on critical velocity in water–$NaMnO_4$ solution, in contrast to the theoretically expected decrease in V as a result of impurity build-up in the contact region due to the screening effect of particles. The relatively large values of G in their experiments conceivably countered the solute effects, leaving no visible effects on V. On the other hand, Sekhar *et al.* [24, 25] found strong effects of impurity on particle trapping mechanisms in directional solidification experiments on SCN when temperature gradient effects were unimportant.

2.5. Geometrical and other effects

The engulfment velocity is a function of shape, size and surface roughness of the particle being engulfed. For a sphere, $V \propto 1/R$, but for a disc in front of a planar front, $V \propto 1/R^3$ [40]. The surface roughness tends to reduce the effective sphere radius compared to a smooth sphere, so that V is increased for rough particles. In the case of composites, the interactions of chemically reactive particles with the melt prior to solidification may lead to surface roughening (together with changes in local solute concentration and surface energies) of initially smooth particles. Natural convection effects may influence the critical velocity for large particles whose dimensions compare with the scale of the hydrodynamic boundary layers (usually 10 to 1000 μm). On the other hand, fine (submicrometre-sized) particles ahead of the front may experience Brownian (thermal) motion. Capture by non-planar (e.g. cellular and dendritic) interfaces during solidification of alloys and solutions is a rule rather than an exception, although no quantitative models are available at present to deal with such interfaces. Under these conditions, the particles may be geometrically entrapped between two or more converging growth fronts (secondaries); in such cases lines of particles decorate cell boundaries, with the separation between particles of the order of the cell dimensions. When the diffusive interactions are strong, the particles may themselves introduce morphological transitions (such as dendrite tip splitting or healing of an initially cellular interface) during growth prior to their capture [24, 25]. At present, only a qualitative understanding of several of these phenomena is available.

3. General observations

Table II summarizes the theoretical models of particle–front interactions, based upon the mechanisms discussed above, that have been proposed in

TABLE II Theoretical models of particle–front interactions

Authors	Main features	Predictions
Uhlmann *et al.* [18] (UCJ)	Repulsive (surface energetic) and attractive (drag) forces introduced; front shape assumed *a priori*; G neglected; several ill-defined length scales. First model to predict V.	$V = \frac{n+1}{2}\left(\frac{L a_0 \Omega D_l}{kTR^2}\right)$; $n \simeq 4$–5
Bolling and Cisse [37] (BC)	More rigorous determination of front shape than UCJ; treatment for smooth and rough particles; curvature-dependent attractive drag force; introduced gravity as correction to drag; some ill-defined parameters; nature of rejection force not clear.	$V \approx \left(\frac{4\Psi(\alpha) kT a_0 \sigma_{SL}}{9\pi\mu^2 R^3}\right)^{1/2}$; $R < R_b$ $V \approx \frac{6\alpha kT\sigma_{SL}}{\pi R^3 R_b g \Delta\rho\mu}$; $R \gg R_b$ $\Psi(\alpha) = \alpha(1-\alpha)^2(\beta - \ln\alpha)$; $\beta \approx 1.0$
Hoekstra and Miller [22] (HM)	Pushing by ice front modelled; rejection force due to change in thickness of transition layer on ice with temperature; effect of G considered.	$V = \frac{2D_l \Delta S G}{k T \rho_s \Delta v}\left(\frac{h_0}{R}\right)$
Chernov *et al.* [32–34] (CTM)	Disjoining pressure as repulsive force; shape preserving paraboloidal front; considers smooth particles and effect of $K_p \neq K_l$; neglects kinetic undercooling.	$V = 0.14 B^{2/3}\sigma_{SL}^{1/3}/\mu R^{4/3}$; $R < 500\,\mu m$ $V = 0.15 B/\mu R l$; $R > 500\,\mu m$ $V = \frac{B}{24\mu R l}\left\{\frac{1+K'}{1-2K'}[9(1-2K')]^{1/4}\right\}$ $K' = (K_l - K_p)/(2K_l + K_p)$; $l = \left(\frac{B\Omega}{\Delta S G}\right)^{1/2}$
Gilpin [31]	Disjoining pressure as repulsive and drag as attractive forces; includes effect of G.	Numerical solution for V
Stefanescu *et al.* [4, 13] (SDKM)	Repulsive surface energetic and attractive drag forces; successive approximation to include buoyancy and thermal conductivity mismatch; introduces effect of finite volume fraction of particles.	$V = \frac{1}{6\mu R}\left[\Delta\sigma_0 \cdot \frac{h_0}{2}\left(2 - \frac{K_p}{K_l}\right) - \frac{4}{3}R^3\Delta\rho g\right]$
Shangguan *et al.* [38] (SAS)	Follows SDKM but more rigorous determination of local shape perturbation in the front; effects of G, buoyancy and $K_p \neq K_l$ considered.	$V = \frac{a_c K_l \Delta\sigma_0}{3\mu K_p (n-1)}\left(\frac{n-1}{n}\right)^n$
Potschke and Rogge [29] (PR)	Repulsive van der Waals and attractive drag forces assumed; both thermal and solute effects considered; does not rely on estimates of zone of strong interactions.	$V = \frac{1.3\Delta\sigma_0}{\mu}\left[16\left(\frac{R}{a_0}\right)^2\left(\frac{K_p}{K_l}\right)\left(15\frac{K_p}{K_l} + x\right) + x^2\right]^{-0.5}$ $x = C_\infty \lvert m_l \rvert \Delta\sigma_0 / K_c G \mu D_l$
Sasikumar *et al.* [35, 36]	Follows CTM; considers $K_p \neq K_l$; deduces front shape under both steady and non-steady state conditions; assumes repulsive van der Waals and attractive drag forces.	Numerical solution for V
Zubko *et al.* [17]	Follow CTM and uses the ratio K_p/K_l to predict pushing–engulfment transitions in several experimental systems; successful in nine out of ten systems.	$\frac{K_p}{K_l} > 1$; capture $\frac{K_p}{K_l} < 1$; rejection
Surappa and Rohatgi [39]	Replaces thermal conductivity ratio in Zubko *et al.*'s criterion by heat diffusivity ratio; successful in all systems to which it has been applied.	$\left(\frac{K_p C_p \rho_p}{K_l C_l \rho_l}\right)^{1/2} > 1$; capture $\left(\frac{K_p C_p \rho_p}{K_l C_l \rho_l}\right)^{1/2} < 1$; rejection
Neumann *et al.* [15, 28]	Qualitative predictions of pushing–engulfment transitions based on a surface thermodynamic criterion; valid at low growth rates and negligible body forces.	$\Delta\sigma_0 < 0$; capture $\Delta\sigma_0 > 0$; rejection $\Delta\sigma_0 = \sigma_{Sp} - (\sigma_{LP} + \sigma_{SL})$

the literature. In spite of the fact that a large number of theoretical models of particle–solidification front interactions are available, only a limited attempt has been made in the past at experimental verification of these models. Thus, Uhlman *et al.* [18] reported a qualitative agreement between their theory and measurements of V in some organic and aqueous systems. Cisse and Bolling [14, 16] reported a fair quantitative agreement between their data in water and Salol matrices and predictions of the Bolling and Cisse (BC) model [37], over a relatively narrow range of particle sizes. On the other hand, Gilpin [31] reported that the large discrepancy between his model and Cisse and Bolling's experimental data [14] was due to a large

variability between different measurements of V in the latter study. Potscke and Rogge [29] reported a good quantitative agreement between their model and the measurements of Korber *et al.* [23] of V in the latex–ice-water system over a relatively narrow range of particle sizes and temperature gradients. No quantitative verification of the CTM model [32–34] appears to have been undertaken, although Zubko *et al.* [17] have successfully demonstrated that the ratio K_p/K_1 can be used in making predictions of pushing–engulfment transitions in various systems. Similarly, limited experimental verification of the SDKM [13] and SAS [38] models and that of Sasikumar *et al.* [35, 36] models has been attempted. Table III gives the ratio of experimental to theoretical velocities for different models, based on their verification against experiments reported in each original study. Most of the theoretical models have been tested against limited data from a single study; a comprehensive evaluation of all major models against published data from different experimental studies was carried out recently [43] with a view to examining the reliability of each model in making predictions of critical velocity. The results showed that the models listed in Table II can be arranged as follows in ascending order of their relative success in correctly predicting the critical velocity: UCJ < HM < BC < PR (SAS) < SDKM < CTM. The evaluation of models attempted [43] is, however, suggestive rather than definitive with respect to its conclusions regarding the predictive capability of each theoretical model. The primary reasons for the qualitative nature of model evaluation attempted [43] are (i) the reported experimental studies did not always rigorously satisfy the assumptions of a particular model (e.g. interface-controlled growth, faceted growth front, smooth particles

TABLE III V_{expt} versus V_{theor} in selected systems

System	Particle diameter (μm)	V_{expt} (μm s^{-1})	V_{theory} (μm s^{-1})
Xylene–water	2.0	13 ± 2	2.5 (UCJ)
	1.0		10 (UCJ)
Solid–water	2.0	7.0	2.5 (UCJ)
	200	0.7	0.6 (UCJ)
SiC–Al	50	8.0 to 400	0.201 (CTM), 0.0119 (BC), 2560 (SDKM)
	150		4.47×10^{-4} (BC)
	200		640 (SDKM)
SiC–SCN	6.0	15	12 (SAS)
	16.0	3.0	5 (SAS)
SiO_2–H_2O	200	0.08	0.006 (Gilpin)
			0.16 (BC)
W–H_2O	5.2	3.3	4.0 (BC)

[a]See Table II for theoretical models.

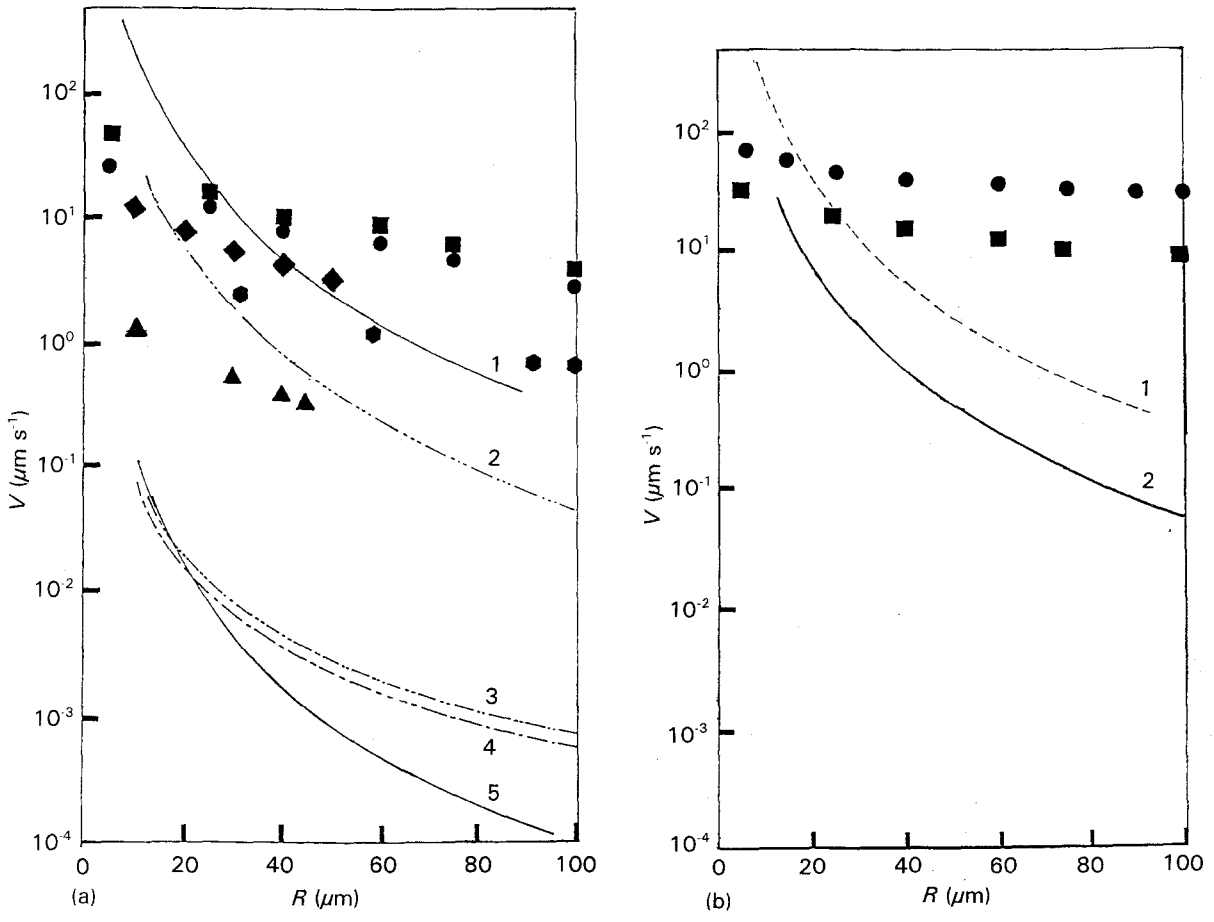

Figure 11 (a) Theoretical velocities (lines) and experimental values (symbols) versus particle radius in several organic systems. (■) Biphenyl–acetal; (4) UCJ, (2) BC. (●) Biphenyl–nylon; (4) UCJ, (1) BC. (◆) Biphenyl–PMMA; (4) UCJ. (◓) Salol–acetal; (5) BC. (▲) Salol–PMMA; (3) UCJ. (b) Theoretical and experimental velocities for naphthalene–particle systems. (■) Naphthalene–nylon; (2) BC. (●) Naphthalene–acetal; (1) BC.

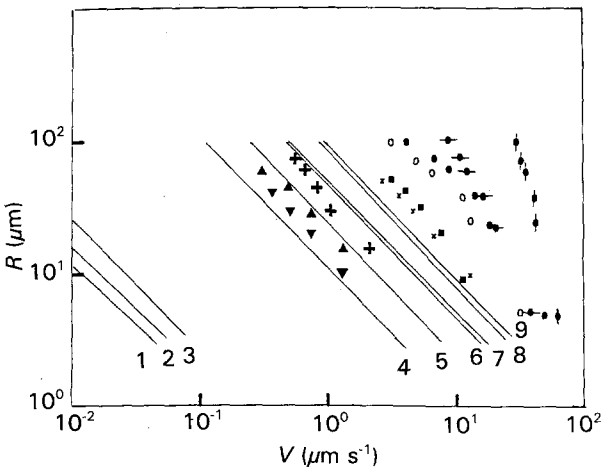

Figure 12 Theoretical predictions (curves 1–9) of V based on the PR model [29] versus experimental data from Neumann and co-workers [15, 28]. (▼) Salol–PMMA, (1); (▲) Salol–nylon, (2); (+) Salol–acetal, (3); (■) biphenyl–PMMA, (4); (×) naphthalene–PMMA, (5); (○) biphenyl–nylon, (6); (●) biphenyl–acetal, (7); (◒) naphthalene–nylon, (8); (◓) naphthalene–acetal, (9).

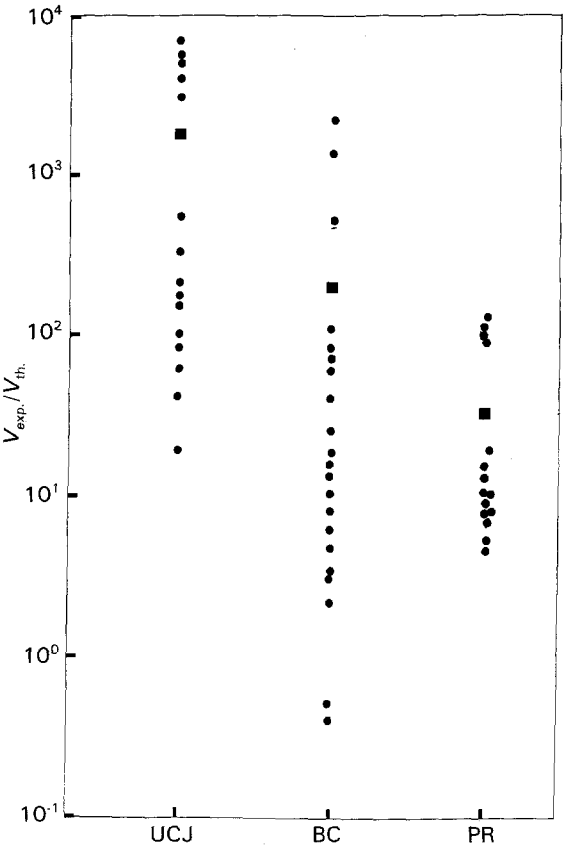

Figure 13 (●) Ratio of experimental to theoretical velocities for UCJ, BC and PR models. The total number of data points tested for each model are 15 for UCJ, 22 for BC and 19 for PR; (■) represents the mean value of the velocity ratio.

etc.), and (ii) uncertainty in the magnitudes of certain material properties, especially surface energies and diffusion coefficients, which make a quantitative validation of each model difficult.

Figs 11 and 12 show a comparison of UCJ, BC and PR models against measurements of critical velocity from the works of Neumann and co-workers [15, 28] in various combinations of salol, biphenyl and naphthalene melts and particles of acetal, nylon, and polymethylmetacrylate (PMMA). The various material property data required in theoretical relationships were obtained from Omenyi *et al.* [28]. Fig. 11 shows that both UCJ and BC models underestimate V, at worst by several orders of magnitude. (A typical value of 5 μm [14] was used for bump radius in the BC model, and although a somewhat better agreement between theory and experiment can be obtained by using a different value of R_b, there is perhaps little basis for assigning numbers to the bump radius in the absence of actual measurements of the wavelength and amplitude of particle surface asperities.) The predictions of the PR model [29] for pure melts have been compared with the data of Neumann and co-workers in Fig. 12 in nine organic systems; the measured V is 5 to 100 times larger than the theoretical velocity, although the theoretically predicted inverse proportionality between V and μ is correctly predicted. The results of the PR model are identical to those of the SAS model [38] for the case of a pure melt and planar front, as can be seen by comparing the relevant equations given in Table II; hence, Fig. 12 identically shows the result for the SAS model. Finally, Fig. 13 plots the ratio of experimental to theoretical critical velocities together with the mean value of the velocity ratio for UCJ, BC and PR (SAS) models. Of the above three models, PR (SAS) is clearly the best choice statistically, with the mean velocity ratios being 32 for PR and over 1900 for UCJ. Also, some of the models (e.g. Hoekstra and Miller's model [22]), which express the critical velocity in terms of the dimension (h_0) of the gap between the particle and the front, often yield values of h_0 (when it is computed using the measured velocities) which should be easily resolved at optical magnifications [43]; however, no observable films (postulated in the models to be about 10^{-6} cm thick) have ever been reported in studies on particle–front interactions, and this casts strong doubt on the validity of such models.

Since sharp transitions in pushing–engulfment behaviour are rarely observed, the identification of a well-defined critical velocity from experimental data for comparison with theoretical models is often difficult. This, together with the difficulty in obtaining accurate measurements or estimates of material properties such as surface energies and diffusion coefficients, makes a reliable comparison of theory and experiments difficult. Consequently, in spite of the availability of theoretical models which predict in a qualitatively correct fashion the effects of various material and geometrical parameters on the critical velocity of particle engulfment, quantitative validation of a particular model may sometimes be difficult. There is clearly a need to generate more extensive and careful data on V under conditions in which a particular model is applicable (e.g. faceted growth front, particles with controlled surface roughness) in order to check the reliability of each model independently. It is also imperative to devise techniques to measure or make reliable predictions of surface energies and other material properties before such an exercise can become reliable. Finally, as shown by recent studies [24,

25], the particles can induce morphological transitions under certain conditions of growth and the trapping mechanisms of particles themselves depend upon the shape of the solidification front (i.e. engulfment by a planar front or geometrical entrapment by a cellular or dendritic interface). It may, therefore, be necessary to combine the fundamental approaches used in the morphological stability theories and the theories of particle–front interactions in order to develop a comprehensive theoretical framework which is valid for a wide variety of materials, ranging from ionic crystals growing from dilute aqueous solutions under interface controlled conditions, to cells and dendrites in concentrated metallic alloys growing under the conditions of simultaneous heat and mass diffusion. Our ability to design microstructures in many modern materials such as discontinuously reinforced cast metal-matrix composites [2–6, 41, 42] critically depends upon our ability to control in a premeditated fashion the interactions of solidifying melts with foreign particles.

References

1. N. L. FRIER, Y. SHIOHARA and K. C. RUSSELL, in Proceedings of MRS International Meeting on Advanced Materials, Vol. 4 (MRS, 1989) p. 47.
2. D. J. LLOYD, *Compos. Sci. Tech.* **35** (1989) 159.
3. J. W. McCOY and F. E. WAWNER, in "Cast Reinforced Metal Composites", edited by S. G. Fishman and A. K. Dhingra (ASM International, Metals Park, OH, 1988) p. 237.
4. D. M. STEFANESCU, B. K. DHINDAW, A. S. KACAR and A. MOITRA, *Metall. Trans.* **19A** (1988) 2847.
5. P. K. ROHATGI, R. ASTHANA and S. DAS, *Int. Mater. Rev.* **31**(3) (1986) 115.
6. P. K. ROHATGI, F. M. YARANDI, Y. LIU and R. ASTHANA, *Mater. Sci. Eng.* **A147** (1991) L1.
7. M. C. FLEMINGS, *Sci. Amer.* **231** (1974) 88.
8. K. H. CHEN and W. R. WILCOX, *J. Cryst. Growth* **40** (1977) 214.
9. V. H. S. KUO and W. R. WILCOX, *Ind. Eng. Chem. Process Des. Dev.* **12** (1973) 376.
10. A. E. CORTE, *J. Geophys. Res*, **67** (1962) 1085.
11. V. L. BRONSTEIN, Y. A. ITKIN and G. S. ISHKOV, *J. Cryst. Growth* **52** (1981) 345.
12. B. K. DHINDAW, A. MOITRA, D. M. STEFANESCU and P. A. CURRERI, *Metall. Trans.* **19A** (1988) 1899.
13. D. M. STEFANESCU, A. MOITRA, A. S. KACAR and B. K. DHINDAW, *ibid.* **21A** (1990) 231.
14. J. CISSE and G. F. BOLLING, *J. Cryst. Growth* **10** (1971) 67.
15. S. N. OMENYI and A. W. NEUMANN, *J. Appl. Phys.* **47** (1976) 3956.
16. J. CISSE and G. F. BOLLING, *J. Cryst. Growth* **11** (1971) 25.
17. A. M. ZUBKO, V. G. LOBANOV and V. V. NIKONOVA, *Sov. Phys. Crystallog.* **18** (1973) 239.
18. D. R. UHLMAN, B. CHALMERS and K. A. JACKSON, *J. Appl. Phys.* **53** (1964) 2986.
19. A. DERUYTTERE, L. FROYEN and S. DEBONDT, *Adv. Space Res.* **6**(5) (1986) 101.
20. B. A. MIKUCKI, S. O. SHOOK, W. E. MERCER II and W. G. GREEN, *Light Metal Age* (October 1986) 16.
21. C. E. SCHEVZOV and F. WEINBERG, *Metall. Trans.* **16B** (1985) 367.
22. P. HOEKSTRA and R. D. MILLER, *J. Coll. Inter. Sci.* **25** (1967) 166.
23. C. KORBER, G. RAU, M. D. COSMAN and E. G. CRAVALHO, *J. Cryst. Growth* **72** (1985) 649.
24. J. A. SEKHAR, R. TRIVEDI and S. H. HAN, in "Solidification of Metal Matrix Composites", edited by P. K. Rohatgi (TMS, 1990) p. 21.
25. J. A. SEKHAR and R. TRIVEDI, *Mater. Sci. Eng.* **A147** (1991) 9.
26. O. P. FEDOROV, *J. Cryst. Growth* **102** (1990) 857.
27. V. Ya. KHAIMOV-MAL'KOV, in "Growth of Crystals" (in Russian), Vol. 2 (Izd. Akad. Nauk. SSSR., 1959) p. 5.
28. S. N. OMENYI, R. P. SMITH and A. W. NEUMANN, *J. Coll. Interf. Sci.* **75** (1980) 117.
29. J. POTSCHKE and V. ROGGE, *J. Cryst. Growth* **94** (1989) 726.
30. A. A. CHERNOV and A. M. MELNIKOVA, *Sov. Phys. Crystallogr.* **10** (1966) 672.
31. R. R. GILPIN, *J. Coll. Interf. Sci.* **68** (1979) 235.
32. A. A. CHERNOV, D. E. TEMKIN and A. M. MELNIKOVA, *Sov. Phys. Crystallogr.* **21** (1976) 369.
33. A. A. CHERNOV and A. M. MELNIKOVA, *ibid.* **10** (1966) 666.
34. A. A. CHERNOV, D. E. TEMKIN and A. M. MELNIKOVA, *ibid.* **22** (1977) 656.
35. R. SASIKUMAR, T. R. RAMAMOHAN and B. C. PAI, *Acta Metall. Mater.* **37** (1989) 2085.
36. R. SASIKUMAR and M. KUMAR, *ibid.* **39** (1991) 2503.
37. G. F. BOLLING and J. CISSE, *J. Cryst. Growth* **10** (1971) 56.
38. D. SHANGGUAN, S. AHUJA and D. M. STEFANESCU, *Metall. Trans.* **23A** (1992) 669.
39. M. K. SURAPPA and P. K. ROHATGI, *J. Mater. Sci.* **16** (1981) 765.
40. P. F. AUBORG, "Interactions of Second Phase Particles with a Crystal Growing from the Melt", PhD Thesis, MIT, Cambridge, Mass. (1978).
41. K. C. RUSSELL, J. A. CORNIE and S. Y. OH, in "Interfaces in Metal Matrix Composites" edited by A. K. Dhingra and S. G. Fishman (TMS/AIME, 1986) p. 61.
42. A. MORTENSEN and I. JIN, *Int. Mater. Rev.* **37**(3) (1992) 101.
43. R. ASTHANA and S. N. TEWARI, *Process. Adv. Mater.* in press.
44. R. M. PILLIAR and J. NUTTING, *Phil. Mag.* **16** (1967) 181.
45. P. K. ROHATGI, S. RAY, R. ASTHANA and C. S. NARENDRANATH, *Mater. Sci. Eng.* in press.
46. P. K. ROHATGI and R. ASTHANA, in "Cast Reinforced Metal Composites", edited by S. G. Fishman and A. K. Dhingra (ASM International, 1988).
47. P. K. ROHATGI, R. ASTHANA, R. N. YADAV and S. RAY, *Metall. Trans.* **21A** (1990) 2073.
48. B. V. DERYAGIN, E. M. LIFSHITZ and L. A. ABRIKOSOVA, *Usp. Fiz. Nauk.* **64** (1958) 493.
49. M. C. FLEMINGS, "Solidification Processing" (McGraw-Hill, 1974).

Received 6 October 1992
and accepted 22 February 1993